Are Binary Black Hole Mergers and Long Gamma-Ray Bursts Drawn from the Same Black Hole Population?

Benjamin Arcier, Jean-Luc Atteia

Benjamin Arcier, Jean-Luc Atteia. Are Binary Black Hole Mergers and Long Gamma-Ray Bursts Drawn from the Same Black Hole Population?. The Astrophysical Journal, 2022, 933 (1), pp.17. ⟨10.3847/1538-4357/ac6604⟩. ⟨hal-03651278⟩

The Astrophysical Journal, 933:17 (14pp), 2022 July 1 https://doi.org/10.3847/1538-4357/ac6604

Are Binary Black Hole Mergers and Long Gamma-Ray Bursts Drawn from the Same Black Hole Population?

Benjamin Arcier and Jean-Luc Atteia
IRAP, Université de Toulouse, CNES, CNRS, UPS, Toulouse, France; Benjamin.Arcier@irap.omp.eu

Received 2021 November 16; revised 2022 March 16; accepted 2022 April 9; published 2022 June 29

Abstract

This paper compares the population of binary black hole (BBH) mergers detected by LIGO/Virgo with selected long gamma-ray burst (GRB) world models convolved with a delay function (LGRBs are used as a tracer of stellar-mass BH formation). The comparison involves the redshift distribution and the fraction of LGRBs required to produce the local rate of BBH mergers. We find that BBH mergers and LGRBs cannot have the same formation history, unless BBH mergers have a long coalescence time of several Gyr. This would imply that BHs born during the peak of long GRB formation at redshift $z \approx 2-3$ merge within the horizon of current GW interferometers. We also show that LGRBs are more numerous than BBH mergers, meaning that most of them do not end their lives in BBH mergers. We interpret these results as an indication that BBH mergers and LGRBs constitute two distinct populations of stellar-mass BHs, with LGRBs being more frequent than BBH mergers. We speculate that the descendants of LGRBs may resemble galactic high-mass X-ray binaries more than BBH mergers. Finally, we discuss the possible existence of a subpopulation of fast-spinning LGRB descendants among BBH mergers, showing that this population, if it exists, is expected to become dominant beyond redshift $z \approx 1$, leading to a change in the observed properties of BBH mergers.

Unified Astronomy Thesaurus concepts: Astrophysical black holes (98); Gamma-ray bursts (629); Gravitational wave sources (677)

1. Introduction

Black hole (BH) astrophysics is a rapidly evolving field, especially thanks to the discovery of dozens of binary black hole (BBH) mergers by the LIGO Scientific Collaboration and Virgo Collaboration (LVC). Despite the apparent simplicity of BHs as astrophysical objects, a global vision of their origin and evolution is still missing, as well as a full understanding of their role in the evolution of the universe and in the formation of its structures. In such a situation, a comparison of the properties of various BH populations may shed light on their common or diverse origins. We focus here on two populations of stellar-mass BHs, which are observed in different contexts: long gamma-ray bursts (long GRBs or LGRBs) and the merges of stellar-mass BHs (BBH mergers).

Long GRBs are the brightest explosions detectable in the electromagnetic domain (e.g., Vedrenne & Atteia 2009; Atteia et al. 2017). They occur when the core of a massive star collapses into a BH or a hypermassive magnetar, subsequently ejecting a transient relativistic jet in our direction. The association of LGRBs with stellar collapse is confirmed by the detection of broad-line core-collapse supernovae (SNe) of Type Ibc a few days after several nearby LGRBs ($z \leqslant 0.3$; Galama et al. 1998; Tagliaferri et al. 2006). However, only a small fraction of core-collapse SNe produce LGRBs.

This fraction has been evaluated by Soderberg et al. (2006b), based on volumetric rates of about 9000 $\mathrm{Gpc^{-3}\,yr^{-1}}$ for SNe Ibc and $f_b \times 1\ \mathrm{Gpc^{-3}\,yr^{-1}}$ for classical LGRBs (e.g., Wanderman & Piran 2010; Palmerio & Daigne 2021), where f_b is the GRB beaming factor. It is difficult to evaluate the true rate of GRBs, due to large uncertainties on the measurements of the beaming angles of GRB jets (thus on f_b). With typical values of f_b in the range 75–250 (corresponding to a jet opening angle in the range 5°–9°), classical LGRBs represent between 1% and 3% of SNe Ibc. This is compatible with another study of Soderberg et al. (2006a), which shows that less than 10% of SNe Ibc are associated with a successful GRB, based on the radio follow-up of 68 local SNe Ibc. We note that this fraction concerns only classical LGRBs, excluding low-luminosity GRBs, which have also been shown to be associated with SNe Ibc, or choked GRBs, whose jets do not pierce the star's envelope. The rate of low-luminosity GRBs is estimated to be ∼100–1000 $\mathrm{Gpc^{-3}\,yr^{-1}}$ (Soderberg et al. 2006b; Liang et al. 2007), comparable or a few times higher than the rate of classical LGRBs. The rate of choked GRBs has not been measured.

The conditions for GRB production by dying massive stars are far from being fully elucidated. MacFadyen & Woosley (1999) emphasized the key role of the angular momentum of the stellar core, which has to be sufficiently large to permit the survival of a massive accretion disk when the BH forms. Before the discovery of BBH mergers with low effective spins by the LVC, it was commonly assumed that GRB progenitors could be single stars with low metallicity, whose weak stellar winds carry away a small fraction of the star angular momentum or stars in binary systems, which are sufficiently close to be tidally locked and keep a high angular momentum (e.g., Woosley & Bloom 2006; Levan et al. 2016; Chrimes et al. 2020). Except for a few events with an associated SN, we have only indirect information about the progenitors of LGRBs, because the information is mediated by the relativistic jet, whose properties are not directly connected with the nature of the progenitor. The population of long GRB progenitors can nevertheless be constrained via statistical studies relying on redshift measurements and the nature of the host galaxies. This has led to the construction of long GRB world models, which describe the history of long GRB formation and are compatible with their observed redshift distributions (Salvaterra et al. 2012; Lien et al. 2014; Palmerio & Daigne 2021).

Contrary to LGRBs, BBH mergers are mostly silent in the electromagnetic domain (see, however, Farris et al. 2010, Bartos et al. 2017, and McKernan et al. 2020 for discussions about the possible emission of electromagnetic transients by BBHs lying in dense gaseous environments). These cataclysmic events, which were discovered by the LVC in 2015 (Abbott et al. 2016), release most of their energy in gravitational waves (GWs). The origins of these BBH mergers are highly debated, and the variety of systems discovered by the LVC probably calls for multiple populations (Wang et al. 2021; Zevin et al. 2021; however, see also Bavera et al. 2020). There is nevertheless a broad consensus that most of the mergers detected by the LVC are of astrophysical origin, even if a marginal contribution from primordial BHs remains possible (De Luca et al. 2021). BBH mergers of astrophysical origin result from the evolution of massive stars, which can be in isolated binary systems or in a dense environment prone to dynamical interactions.

Considering the different biases affecting the detection of BBH mergers and LGRBs, a comparison of these two populations is likely to shed new light on the origin and evolution of stellar-mass BHs of astrophysical origin.

In this article, we compare the basic statistics concerning these two populations. First, a $V/V_{\rm max}$ test is used to compare the redshift distributions of BBH mergers with various delayed long GRB models, where the long GRB models are used as proxies for the formation history of stellar-mass BHs. This comparison, which takes into account the shape of the redshift evolution independent of the normalization of the two populations, leads us to identify several compatible models that can reproduce the redshift distributions of the BBH mergers detected by LVC. In a second step, we compare the rate of BBH mergers measured by LVC with the rate of long GRBs. This comparison makes no assumption of a physical connection between the two populations; it only uses the rate of the long GRBs as a useful reference point for the comparison of populations with different redshift evolutions. We find that the progenitors of BBH mergers are rare compared with GRBs. For these two studies, the BBH mergers are considered as a single population.

These findings are then briefly discussed in the context of models developed to explain the BBH mergers and GRBs. Emphasizing the potential role of tidal spin-up for both types of sources, we show that present data allow for the existence of a minority of fast-spinning BBH mergers that quickly follow the production of LGRBs.

This study has been made possible by the publication of the GWTC-2 and GWTC-3 catalogs obtained with the O3 observing run (Abbott et al. 2021a; The LIGO Scientific Collaboration et al. 2021b). These catalogs contain 79 BBH mergers with redshifts ranging from $z = 0.05$ to $z = 0.82$, with a median of $z = 0.3$, enabling a comparison of the redshift distributions of BBH mergers and GRBs over the last 7 Gyr. It follows a first work from Atteia et al. (2018), which was based on the GWTC-1 catalog (Abbott et al. 2019) and thus limited to a rate comparison of BBHs and LGRBs.

This paper is organized as follows. In the next two sections, we compare the redshift distributions (Section 2) and the volumetric rates (Section 3) of BBH mergers and LGRBs. Then, in Section 4, we briefly discuss the implications of these results in the context of stellar evolution models developed to explain LGRBs and BBH mergers.

Throughout this paper, we use a flat Λ cold dark matter cosmological model with the parameters measured by the Planck Collaboration: $H_0 = 67.4\,{\rm km\,s^{-1}\,Mpc^{-1}}$ and $\Omega_{\rm m} = 0.315$ (Planck Collaboration et al. 2020).

2. Redshift Distribution

The fast-growing number of BBH mergers detected by the LVC provides some indications of their redshift distribution, as discussed in Abbott et al. (2021b) and The LIGO Scientific Collaboration et al. (2021a). Using a generalization of the $V/V_{\rm max}$ test developed by Schmidt (1968), we compare here the redshift distribution of 79 BBH mergers detected with high confidence by the LVC with three recent models of classical LGRBs and one star formation history (SFH) model.

2.1. Methodology

We use a test called $N/N_{\rm max}$, which is a variant of the $V/V_{\rm max}$ test developed by Schmidt (1968). These tests are used to assess the compatibility of the volumetric distribution of observed sources with a model. In the $V/V_{\rm max}$ test, the model is used to compute, for each source, the ratio of the volume enclosed by the source to the maximum volume of detection for this source. If the model is correct, the source is randomly chosen among all visible sources and the ratio $V/V_{\rm max}$ follows a uniform distribution $\mathcal{U}(0,\,1)$. In its simplest form, the $V/V_{\rm max}$ test considers sources without cosmological evolution. For sources with cosmological evolution, the test can be adapted by considering the ratio of the predicted number of sources within the volume enclosed by a source to the number of sources within the maximum volume of detection for this source. When the model is completely defined and the volume of detection is correctly calculated, the $V/V_{\rm max}$ and $N/N_{\rm max}$ tests are hardly affected by selection effects, because each source is placed within its own volume of detection.

The volume of detection of each BBH merger is computed via the determination of its *horizon* $z_{\rm h,i}$, which is the maximum redshift at which this merger could be detected (see below). Knowing the merger event redshift $z_{\rm i}$ and its horizon redshift $z_{\rm h,i}$, we can compute $N_{\rm i}$, the number of sources closer than $z_{\rm i}$, and $N_{\rm max,i}$, the number of sources closer than the horizon $z_{\rm h,i}$, for various source models. A model is acceptable if the ratio $N_{\rm i}/N_{\rm max,i}$ follows a uniform distribution $\mathcal{U}(0,\,1)$. The agreement of the distribution of $N_{\rm i}/N_{\rm max,i}$ with $\mathcal{U}(0,\,1)$ is evaluated with a Kolmogorov–Smirnov test (hereafter, KS test). This comparison does not take into account the normalization of the GRB and BBH merger rates, which is discussed in Section 3.

The method used to determine the horizon redshift is based on the horizon calculation method proposed in Chen et al. (2021), using the open source code that is available online.[1] The equation for computing the signal-to-noise (S/N)

---

[1] https://github.com/hsinyuc/distancetool

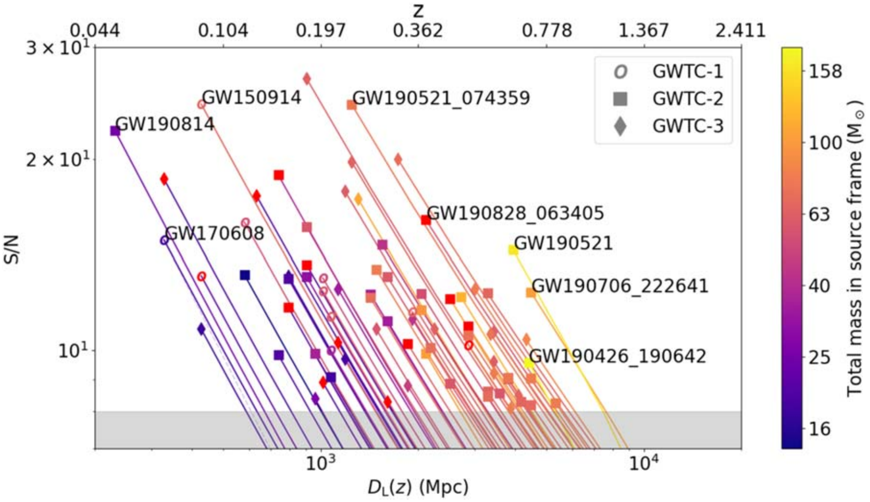

Figure 1. S/N dependence on redshift for the BBH mergers observed during O1, O2, O3a, and O3b. The color coding represents the total mass of the binary in the observer frame, while the marker styles represent the catalogs in which the events are listed. The dashed line for GW170608 illustrates an S/N dependency inversely proportional to the luminosity distance.

evolution with the redshift is taken from Chen et al. (2021):

$$\mathrm{S/N_{Ch21}} = \sqrt{4 \int_{f_{\min}}^{f_{\max}} \frac{|h^{+}(f)|^2}{S_{\rm h}(f)} {\rm d}f}, \quad (1)$$

where $h^+(f)$ is the plus polarization of the GW merger and $S_{\rm h}(f)$ is the power-spectral density of the interferometer. The calculation of $h^+(f)$ depends on the binary properties and its relative distance to the observer, in addition to the masses m_1 and m_2 of the BBH merger components. The plus polarization is obtained using the `lalsimulation` Python package with the waveform *IMRPhenomD* (as also for the online calculator provided by Chen et al. 2021, since m_1 or $m_2 \geqslant 3\,M_\odot$). For the term $S_{\rm h}(f)$, we took the same strain noise curve for LIGO Handford and LIGO Livingston, for a given observing run, already included in the Github repository by Chen et al. (2021).

Contrary to Chen et al. (2021), who define the horizon as the highest redshift at which a BBH merger could be detected with the best antenna pattern (considering that the BBH system is optimally oriented relative to the GW detectors and located in a portion of the sky where the interferometer performance is at a maximum), we define the horizon as the maximum redshift at which a BBH merger would be detected *under the conditions of its detection*. Since the antenna pattern does not depend upon distance and cosmology, it is possible to normalize the S/N dependence on redshift with the actual ratio, $\mathrm{S/N_0}$, obtained for a given merger detected at redshift z_0. We obtain the S/N dependence on redshift corrected by the antenna pattern, allowing the computation of the horizon redshift for each detected merger:

$$\mathrm{S/N}(z, m_1, m_2) = \frac{\mathrm{S/N_{Ch21}}(z, m_1, m_2)}{\mathrm{S/N_{Ch21}}(z_0, m_1, m_2)} \times \mathrm{S/N_0}. \quad (2)$$

Taking a threshold $\mathrm{S/N_{lim}}$, the horizon redshift is the variable $z_{\rm h,i}$, solving the equation:

$$\mathrm{S/N}(z_{\rm h,i}, m_1, m_2) = \mathrm{S/N_{lim}}. \quad (3)$$

The S/N, mass, and detected redshift are taken from the Gravitational Wave Open Science Center event list,[2] created from the GWTC catalogs (Abbott et al. 2019, 2021a; The LIGO Scientific Collaboration et al. 2021b, 2021c). In the following, we consider $\mathrm{S/N_{lim}} = 8$, in agreement with the smallest S/N observed for BBH mergers (Abbott et al. 2019, 2021a), and with the theoretical sensitivities of LIGO/Virgo (Abbott et al. 2018). Recent merger observations from the deep extended catalog from O3a (The LIGO Scientific Collaboration et al. 2021c) and from GWTC-3 (The LIGO Scientific Collaboration et al. 2021b) have detected events with a network matched-filter S/N below this limit, however. These events are not considered in this study. Events with mass m_1 and/or m_2 below 2.4 $M_\odot$ have also been removed, to prevent the contamination from neutron star (NS)–NS or NS–BH merger events.

The Appendix gives the horizons of the 79 events used in this article, computed with this method. Figure 1 illustrates the redshift dependence and the impact of the shape of the LIGO power-spectral density (which is not exactly flat), which causes the departure from the inverse luminosity distance law (shown with a faint dashed line for GW170608). The mergers in GWTC-1, GWTC-2, and GWTC-3 have a broad range of horizons, from $z = 0.12$ to $z = 1.10$, with a median of $z = 0.50$. This is the reflection of their mass range, which spans over 1 decade. This broad range of horizons implies very different detection volumes for massive ($\sim 160\,M_\odot$) and less massive BBH mergers ($\leqslant 20\,M_\odot$), and a mass distribution of detected mergers that is strongly biased in favor of massive BBHs. By construction, the $N/N_{\rm max}$ test takes into account this bias by considering the individual contribution of each BBH merger within its own volume of detection.

The $N/N_{\rm max}$ test requires computing $N_{\rm i}$, the number of mergers expected up to redshift $z_{\rm i}$, and $N_{\rm max,i}$, the number of mergers expected up to redshift $z_{\rm h,i}$. This is based on a world model of a source population that specifies $\rho(z)$, the evolution of the source density rate with redshift. $N_{\rm i}$ is computed as follows:

$$N_{\rm i} = \int_0^{z_{\rm i}} \rho(z)\, \frac{{\rm d}V(z)}{{\rm d}z}\, \frac{1}{1+z}\, {\rm d}z, \quad (4)$$

where $\rho(z)$ is the BBH merger density rate (in $\mathrm{Gpc^{-3}\,yr^{-1}}$), ${\rm d}V(z)$ is the differential comoving volume, and the term

---

[2] https://www.gw-openscience.org/eventapi/html/GWTC/

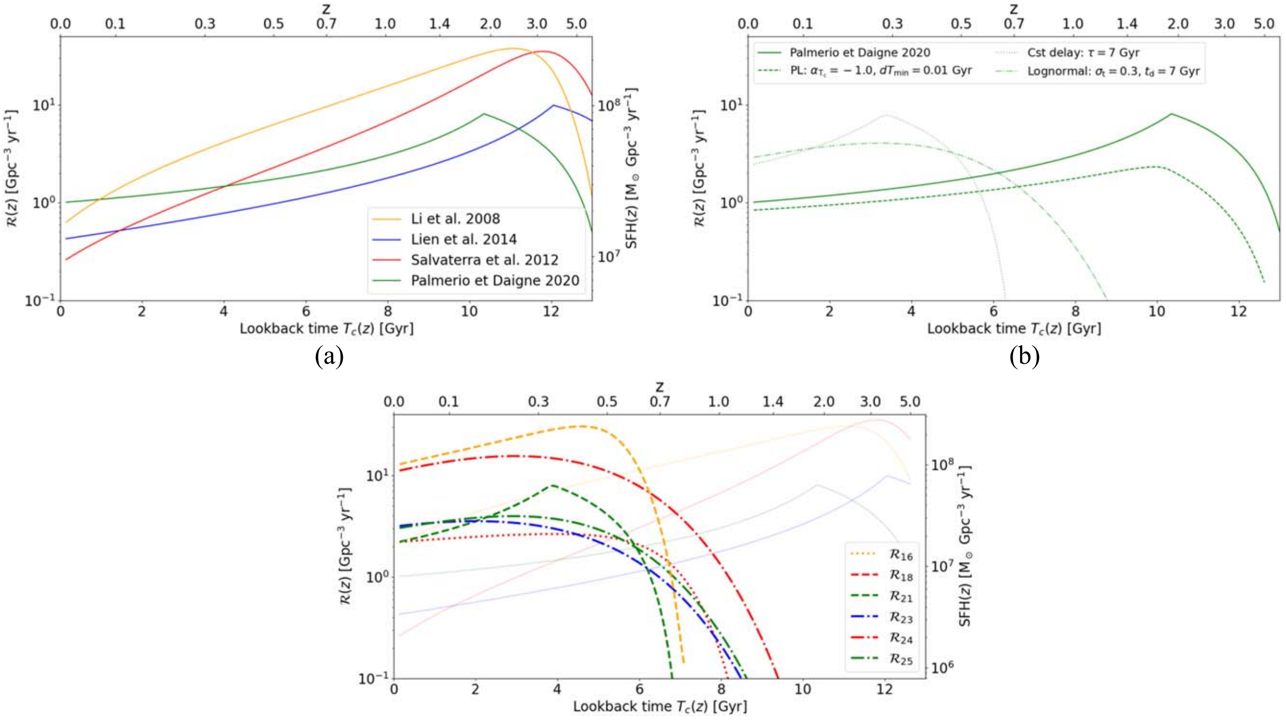

(a) (b)

(c)

Figure 2. GRB density rate models and SFH evolution with redshift, including several time-delay functions. Panel (a): GRB density rates for the three GRB world models (blue, red, and green) and the SFH (orange). Panel (b): the GRB density rate obtained from Palmerio & Daigne (2021) convolved with three shapes of the delay function: the dotted line is for the power-law shape, the dashed line is for the constant delay shape, and the dashed–dotted line is for the lognormal shape. Panel (c): some models with a p-value above 0.1 (dotted and dashed lines). The corresponding models can be found in Table 1. The faint full-line plots are the GRB/SFH models before the delay function convolution.

$1/(1+z)$ accounts for the impact of time dilation when we measure the *rate* of the events (Mao & Paczynski 1992).

We compare here the observed distribution of the BBH mergers with several density rate models: a constant rate model, a model of the SFH, and three GRB world models, which all reproduce the observed properties of the GRBs detected by the Swift and Fermi missions. These three models and the SFH are illustrated in Figure 2(a).

The first GRB model is proposed by Salvaterra et al. (2012):

$$\mathcal{R}^{\mathrm{S}}_{\mathrm{GRB}}(z) = \mathcal{R}^{\mathrm{S}}_0\,(1+z)^{\delta_{\mathrm{n}}}\,\Sigma^{\mathrm{Li}}_{\mathrm{SFH}}(z), \tag{5}$$

based on the cosmic SFH rate from Li (2008):

$$\Sigma^{\mathrm{Li}}_{\mathrm{SFH}}(z) = \frac{a+bz}{1+(z/c)^d}, \tag{6}$$

with $\mathcal{R}^{\mathrm{S}}_0 = 0.24$ Gpc^{-3} yr^{-1}, $\delta_n = 1.7$, $a = 0.0158$, $b = 0.118$, $c = 3.23$, and $d = 4.66$.

The second is proposed by Lien et al. (2014):

$$\mathcal{R}^{\mathrm{L}}_{\mathrm{GRB}}(z) = \mathcal{R}^{\mathrm{S}}_0 \begin{cases} (1+z)^{N_1} & \text{if } z < \mathrm{z}_1 \\ (1+\mathrm{z}_1)^{(\mathrm{n}_1-\mathrm{n}_2)}(1+z)^{N_2} & \text{if } z \geqslant \mathrm{z}_1 \end{cases}, \tag{7}$$

with $\mathcal{R}^{\mathrm{L}}_0 = 0.42$ Gpc^{-3} yr^{-1}, $n_1 = 2.07$, $n_2 = -0.7$, and $\mathrm{z}_1 = 3.6$.

The third is proposed by Palmerio & Daigne (2021):

$$\mathcal{R}^{\mathrm{P}}_{\mathrm{GRB}}(z) = \mathcal{R}^{\mathrm{P}}_0 \begin{cases} e^{az} & \text{if} z < \mathrm{z}_{\mathrm{m}} \\ e^{(a-b)\mathrm{z}_{\mathrm{m}}} e^{bz} & \text{if } z \geqslant \mathrm{z}_{\mathrm{m}} \end{cases}, \tag{8}$$

with $\mathcal{R}^{\mathrm{P}}_0 = 1.0$ Gpc^{-3} yr^{-1}, $a = 1.1$, $b = -0.57$, and $\mathrm{z}_{\mathrm{m}} = 1.9$.

Since the population of BBH mergers probably does not directly trace the GRB population, we also consider delayed models, with a delay function between the GRB emission (when the BH is created) and the transient GW emission (when the BH merges with its companion). This approach is similar to the studies that compare the rates of binary NS mergers and short GRBs (Nakar 2007; Wanderman & Piran 2015). Considering a time-delay probability density function $f(\tau)$, and integrating over all possible time delays, the calculation of the BBH merger rate at redshift z_0 becomes:

$$\rho(z_0) \propto \int_{z_0}^{\infty} \mathcal{R}_{\mathrm{GRB}}(z)\, f(T_c(z) - T_c(z_0))\, \frac{\mathrm{d}T_c}{\mathrm{d}z}\,\mathrm{d}z, \tag{9}$$

where $T_c(z)$ is the lookback time at redshift z and $\tau = T_c(z) - T_c(z_0)$ is the time delay in Gyr between a GRB at redshift z and a merger produced at redshift $z_0 < z$. In practice, a limiting redshift $z_{\mathrm{lim}} = 20$ has been chosen for the calculation of the integral, and we have verified that changing this value from 20 to 100 has no significant impact on the results. The delay function $f(\tau)$ can have several shapes, and in the following we consider three of them: a power law, a lognormal distribution, and a constant delay.

The power law has two parameters: a negative slope α (for example, $\alpha = -1$ in Belczynski et al. 2016) and a minimum merging time $dT_{\min}$. It is described by:

$$f(\tau) = \begin{cases} 0 & \tau \leqslant dT_{\min} \\ \tau^{\alpha} & \tau > dT_{\min} \end{cases}. \tag{10}$$

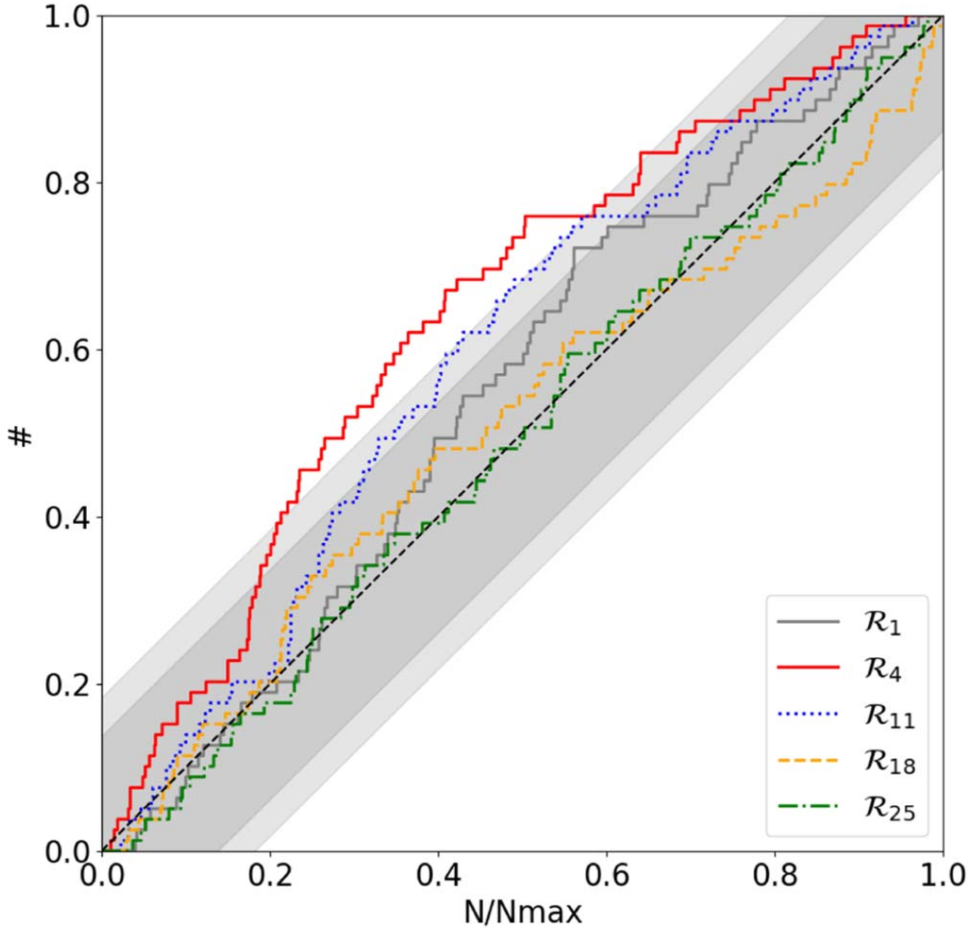

Figure 3. Comparison of $\mathrm{N/N_{max}}$ cumulative distributions with the expected $\mathcal{U}(0,\,1)$ distribution. The shaded areas represent the 1% and 10% acceptance regions for the KS test. $\mathcal{R}_1$ represents the constant model; $\mathcal{R}_4$ the GRB model from Salvaterra et al. (2012); $\mathcal{R}_{11}$ the GRB model from Lien et al. (2014), convolved with a power-law delay function (with $\alpha = -2$ and $dT_{\min} = 0.01$ Gyr); $\mathcal{R}_{18}$ the SFH from Li (2008), with a constant delay of 6.5 Gyr; and $\mathcal{R}_{25}$ the GRB model from Palmerio & Daigne (2021), convolved with a lognormal delay function (with $\mathrm{t_d} = 7.3$ Gyr and $\sigma_{\mathrm{t}} = 0.3$).

The lognormal distribution of width σ_{t} centered around a time delay t_{d} is described by:

$$f(\tau) = \frac{1}{\tau\sigma_{\mathrm{t}}\sqrt{2\pi}}\exp\left(-\frac{\ln(\tau/t_{\mathrm{d}})^2}{2\sigma_{\mathrm{t}}^2}\right). \tag{11}$$

The constant delay is modeled by setting a small dispersion of the lognormal distribution (typically $\sigma_{\mathrm{t}} = 0.01$). This is how the constant delay GRB density rate presented in Figure 2(b) has been created. From the GWTC-1, GWTC-2, and GWTC-3 catalogs, the maximum redshift observed for a BBH merger is $z = 0.71$, which represents a lookback time of ~6.5 Gyr, with the cosmology used in this paper. For this reason, we have not considered constant delay models with a delay greater than 7 Gyr, which would lead to the most distant BBH mergers being produced before the big bang. The differential of the lookback time at redshift z is calculated using the definition of lookback time in Condon & Matthews (2018):

$$\frac{\mathrm{d}T_{\mathrm{c}}}{\mathrm{d}z}(z) = \frac{1}{H(z)(1+z)}. \tag{12}$$

Figure 2(b) illustrates the impact of these different delay functions on the GRB model of Palmerio & Daigne (2021).

2.2. Results

Using the $N/N_{\max}$ test defined in the previous section, we now compare the redshift distribution of the BBH mergers in the GWTC catalogs with various delayed GRB models. A model is considered acceptable if the KS test gives a p-value larger than 1%, and favored if the p-value exceeds 10%. This is illustrated in Figure 3, which compares the cumulative $N/N_{\max}$ distributions of various models with the data. The light gray zone indicates the 99% confidence region, while the dark gray zone shows the 90% confidence interval: a model is accepted at a given confidence level if its $N/N_{\max}$ cumulative distribution function lies entirely inside the gray zone.

The values of $\langle \mathrm{N/N_{max}} \rangle$, the mean of the $N/N_{\max}$ distribution, and the p-values of the KS test are given in Table 1 for selected models. The first five models include a constant density rate evolution in addition to the SFH and the three GRB models presented in the methodology section, without any delay. They are followed by 12 models with a power-law delay function, with two values of the power-law index, $\alpha = -2$, and $\alpha = -1$, and two values of $dT_{\min}$, 0.01 and 5 Gyr. The first value of $dT_{\min}$ is standard for such models, while larger values of this parameter have been used to explore its impact on the density rate distributions. Finally, we also consider 12 models with a lognormal delay function, with three values of the dispersion: $\sigma_{\mathrm{t}} = 0.01$, 0.3, and 1.0—and for each of them we

Table 1
Results of the KS Test for Various Population Models (See Text)

#	Population Model	Delay Parameters	p-value	$\langle N/N_{\max}\rangle$	Figure
$\mathcal{R}_1$	Constant	...	0.035	0.452	3
$\mathcal{R}_2$	SFH: Li (2008)	...	0.001	0.389	2(a), 3
$\mathcal{R}_3$	GRB: Lien et al. (2014)	...	0.005	0.406	2(a)
$\mathcal{R}_4$	GRB: Salvaterra et al. (2012)	...	0.000	0.356	2(a)
$\mathcal{R}_5$	GRB: Palmerio & Daigne (2021)	...	0.014	0.417	2(a), 2(b)
$\mathcal{R}_6$	SFH: Li (2008)	PL, $dT_{\min} = 0.01$ Gyr, $\alpha = -1.0$	0.006	0.412	...
$\mathcal{R}_7$	GRB: Lien et al. (2014)	PL, $dT_{\min} = 0.01$ Gyr, $\alpha = -1.0$	0.012	0.419	3
$\mathcal{R}_8$	GRB: Salvaterra et al. (2012)	PL, $dT_{\min} = 0.01$ Gyr, $\alpha = -1.0$	0.003	0.401	...
$\mathcal{R}_9$	GRB: Palmerio & Daigne (2021)	PL, $dT_{\min} = 0.01$ Gyr, $\alpha = -1.0$	0.017	0.425	2(b)
$\mathcal{R}_{10}$	SFH: Li (2008)	PL, $dT_{\min} = 0.01$ Gyr, $\alpha = -2.0$	0.001	0.390	...
$\mathcal{R}_{11}$	GRB: Lien et al. (2014)	PL, $dT_{\min} = 0.01$ Gyr, $\alpha = -2.0$	0.005	0.406	...
$\mathcal{R}_{12}$	GRB: Salvaterra et al. (2012)	PL, $dT_{\min} = 0.01$ Gyr, $\alpha = -2.0$	0.000	0.357	...
$\mathcal{R}_{13}$	GRB: Palmerio & Daigne (2021)	PL, $dT_{\min} = 0.01$ Gyr, $\alpha = -2.0$	0.014	0.417	...
$\mathcal{R}_{14}$	SFH: Li (2008)	PL, $dT_{\min} = 5.0$ Gyr, $\alpha = -1.0$	0.799	0.517	...
$\mathcal{R}_{15}$	GRB: Lien et al. (2014)	PL, $dT_{\min} = 5.0$ Gyr, $\alpha = -1.0$	0.144	0.463	2(c)
$\mathcal{R}_{16}$	GRB: Salvaterra et al. (2012)	PL, $dT_{\min} = 5.0$ Gyr, $\alpha = -1.0$	0.325	0.476	...
$\mathcal{R}_{17}$	GRB: Palmerio & Daigne (2021)	PL, $dT_{\min} = 5.0$ Gyr, $\alpha = -1.0$	0.676	0.524	...
$\mathcal{R}_{18}$	SFH: Li (2008)	Cst Delay, $\tau = 6.5$ Gyr	0.533	0.494	3
$\mathcal{R}_{19}$	GRB: Lien et al. (2014)	Cst Delay, $\tau = 7.0$ Gyr	0.014	0.422	...
$\mathcal{R}_{20}$	GRB: Salvaterra et al. (2012)	Cst Delay, $\tau = 7.0$ Gyr	0.035	0.458	2(c)
$\mathcal{R}_{21}$	GRB: Palmerio & Daigne (2021)	Cst Delay, $\tau = 6.5$ Gyr	0.255	0.502	2(b), 2(c)
$\mathcal{R}_{22}$	SFH: Li (2008)	logNorm, $t_{\rm d} = 7.3$ Gyr, $\sigma_t = 0.3$	0.966	0.499	...
$\mathcal{R}_{23}$	GRB: Lien et al. (2014)	logNorm, $t_{\rm d} = 10.0$ Gyr, $\sigma_t = 0.3$	0.892	0.519	2(c)
$\mathcal{R}_{24}$	GRB: Salvaterra et al. (2012)	logNorm, $t_{\rm d} = 8.6$ Gyr, $\sigma_t = 0.3$	0.990	0.498	...
$\mathcal{R}_{25}$	GRB: Palmerio & Daigne (2021)	logNorm, $t_{\rm d} = 7.3$ Gyr, $\sigma_t = 0.3$	0.986	0.504	2(b), 2(c), 3
$\mathcal{R}_{26}$	SFH: Li (2008)	logNorm, $t_{\rm d} = 5.0$ Gyr, $\sigma_t = 1.0$	0.023	0.437	...
$\mathcal{R}_{27}$	GRB: Lien et al. (2014)	logNorm, $t_{\rm d} = 5.0$ Gyr, $\sigma_t = 1.0$	0.012	0.424	...
$\mathcal{R}_{28}$	GRB: Salvaterra et al. (2012)	logNorm, $t_{\rm d} = 5.0$ Gyr, $\sigma_t = 1.0$	0.007	0.416	...
$\mathcal{R}_{29}$	GRB: Palmerio & Daigne (2021)	logNorm, $t_{\rm d} = 5.0$ Gyr, $\sigma_t = 1.0$	0.017	0.436	...

Note. The p-values of the favored models are indicated in boldface.

indicate the delay $t_{\rm d}$ that gives the largest p-value. As explained before, the model with $\sigma_{\rm t} = 0.01$ is equivalent to a constant delay model.

According to Table 1, ten models have p-values larger than 10% (the favored models), while 11 models have p-values between 1% and 10%. All the favored models are delayed models, with a significant delay between the GRB and the merger event.

1. The SFH model and the GRB models of Salvaterra et al. (2012), Lien et al. (2014), and Palmerio & Daigne (2021), convolved with a power-law delay function with $\alpha = -1$ and $dT_{\min} = 5$ Gyr ($\mathcal{R}_{14}$, $\mathcal{R}_{15}$, $\mathcal{R}_{16}$, and $\mathcal{R}_{17}$).
2. The SFH model and the GRB model of Palmerio & Daigne (2021), convolved with a constant delay function of 7 Gyr ($\mathcal{R}_{18}$ and $\mathcal{R}_{21}$).
3. The SFH model and the GRB models of Lien et al. (2014), Salvaterra et al. (2012), and Palmerio & Daigne (2021), convolved with a lognormal delay function with $\sigma_{\rm t} = 0.1$ or 0.3 and optimal $t_{\rm d}$ values ($\mathcal{R}_{22}$, $\mathcal{R}_{23}$, $\mathcal{R}_{24}$, and $\mathcal{R}_{25}$).

Some of the favored models are shown in Figure 2(c)—for instance, the model of Lien et al. (2014), with a delay $t_{\rm d} = 10$ Gyr and a dispersion $\sigma_{\rm t} = 0.3$ ($\mathcal{R}_{23}$). A common feature of these models is the decreasing density of mergers beyond $z \approx 0.8$. This is due to the fact that the temporal delay between the GRB and the merger transforms the peak of the GRB production (at $z \approx 2$–3) into a peak of the merger production, at $z \approx 0.5$.

Regarding the models that are not favored (that are rejected or simply not acceptable), they all have values of $\langle N/N_{\max}\rangle$ below 0.5, indicating that they predict too many distant BBH mergers, compared with the GW observations. This is well illustrated by the cumulative distribution function of $N/N_{\max}$ for the models $\mathcal{R}_4$ and $\mathcal{R}_{11}$ in Figure 3.

Figure 4 provides insights into the impact of the delays for the three delay functions studied here, emphasizing some trends: (i) SFH or GRB populations with no delay or a short delay are not favored; (ii) when a delay is included, the three delay functions can reproduce the observed distribution if the delay is sufficiently large—larger than ~6 Gyr for the constant and lognormal delay functions, and $dT_{\min}$ larger than ~4 Gyr for the power-law delay function; (iii) delays with a broad distribution (e.g., a lognormal distribution with $\sigma_{\rm t} = 1$ or a power-law distribution with $dT_{\min}$ smaller than 4 Gyr) are not favored; and, finally, (iv) the crucial parameter for the power-law distribution is $dT_{\min}$, with the slope playing a marginal role.

2.3. Impact of Systematics

These conclusions rely on the accuracy of the redshift measurement by LVC and on the calculation of the merger horizon.

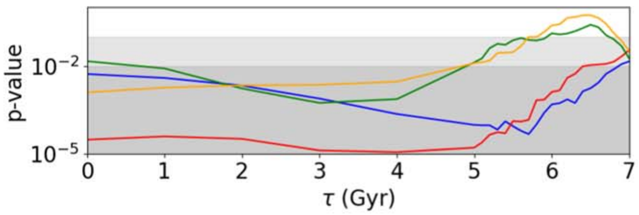

(a) Constant delay function

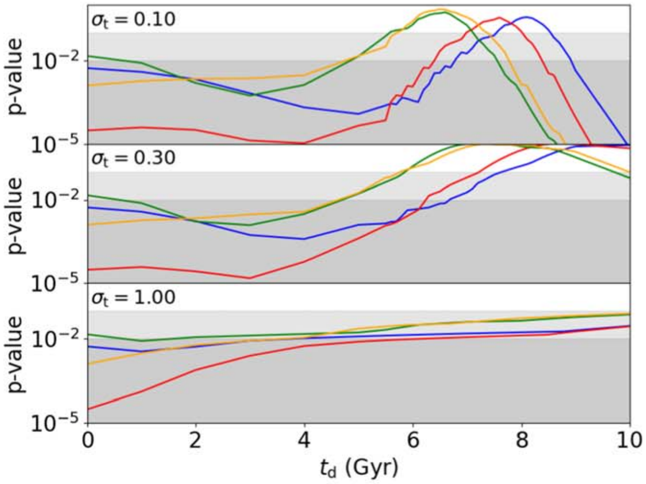

(b) Lognormal delay function

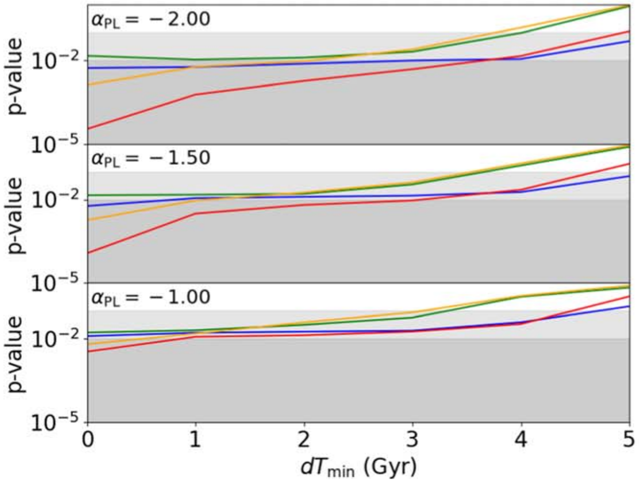

(c) Power-Law delay function

Figure 4. The evolutions of the p-values with the delay, for the various delay functions applied to the three GRB world models considered in the paper (blue, red, and green for, respectively, Salvaterra et al. 2012, Lien et al. 2014, and Palmerio & Daigne 2021), with the SFH from Li (2008) in orange. The light gray and dark gray shaded areas represent the p-value thresholds for the accepted and favored models, set to 1% and 10%, respectively.

The effect of the redshift uncertainties on the p-values has been investigated using the redshift limits given in GWTC-1, GWTC-2, and GWTC-3. The redshifts of the BBH mergers are poorly constrained in these catalogs, with a relative median redshift uncertainty of 39%. We have randomized the redshift values given in the catalog (assuming that the incertitude on the redshift could be modeled by two half-Gaussian distributions whose standard deviations are equal to the 90% confidence interval divided by 1.65) and tested the p-value obtained for each model 10,000 times. Figure 5 shows the 90% confidence interval obtained for the p-values of a given model. When the redshift uncertainty is taken into account, the accepted models $\mathcal{R}_5$, $\mathcal{R}_7$, $\mathcal{R}_9$, $\mathcal{R}_{13}$, $\mathcal{R}_{19}$, $\mathcal{R}_{20}$, $\mathcal{R}_{27}$, and $\mathcal{R}_{29}$ can be rejected for some redshift cases, while the models $\mathcal{R}_6$ and $\mathcal{R}_{28}$ become acceptable. These models are referred to as being marginally acceptable throughout the remainder of the paper. The list of favored models does not change, except for models $\mathcal{R}_{15}$, $\mathcal{R}_{18}$, and $\mathcal{R}_{21}$, which only become acceptable for some cases. These models are referred to as being marginally favored throughout the remainder of the paper.

We conclude that our study is marginally sensitive to statistical uncertainties on the measured merger redshifts. The findings of this article, discussed in the next section, are mainly limited by the number of BBH mergers detected until now.

3. The Rate of BBHs

In this section, we evaluate the density rate of the BBH merger progenitors necessary to produce the BBH merger density rate observed by LVC, considering the favored and marginally favored models identified in Section 2 (with p-values larger than 10%). This density rate will be expressed in terms of the LGRB density rate; the models using the SFH density rate evolution are therefore not considered here. Using the LGRB density rate as a reference does not imply a connection between LGRBs and BBH mergers; this is just a convenient way of specifying the density rate. We defer the discussion of the possible connections between the two populations to Section 4.

3.1. Methodology

Following the approach of Equation 9, we write the expected rate of the BBH mergers $\rho(z_0)$ as a function of their birth rate $\mathcal{R}_{\mathrm{BBHs}}(z)$ and the normalized delay distribution $f(z, z_0)$:

$$\rho(z_0) = \int_{z_0}^{\infty} \mathcal{R}_{\mathrm{BBHs}}(z)\, f(z, z_0) \frac{dT_c}{dz} dz. \tag{13}$$

The best measurement of the BBH merger density rate in GWTC-3 (The LIGO Scientific Collaboration et al. 2021a) occurs at $z = 0.2$. For this reason, the equation above will be computed at $z_0 = 0.2$ to obtain as precise an estimation of the fraction as possible. Using the LGRB rate as a reference, the BBH birth rate $\mathcal{R}_{\mathrm{BBHs}}(z)$ can be linked to the observed LGRB rate using two factors, f_b and η_0:

$$\mathcal{R}_{\mathrm{BBHs}}(z) = \eta_0 \times f_b \times \mathcal{R}_{\mathrm{GRB}}(z). \tag{14}$$

The beaming factor f_b represents the ratio of the total number of LGRBs to the number of *detected* LGRBs pointing toward us. It is sometimes expressed relative to the jet opening angle θ, as $f_b = (1 - \cos\theta)^{-1}$. It is assumed to be independent of redshift.

The parameter η_0 is a normalization factor to be applied to the LGRB density rate to reproduce the observed rate of BBH mergers. η_0 is the number that we aim to constrain in this section, as it permits the comparison of the relative rates of BBH mergers and LGRBs. η_0 has been assumed to be constant and independent of redshift in this analysis. However, it is also possible to assume a difference in evolution between massive BBHs and GRBs, favoring or disfavoring the production of BBH systems relative to the LGRBs. This evolution can follow a simple parameterization of the density population (e.g.,

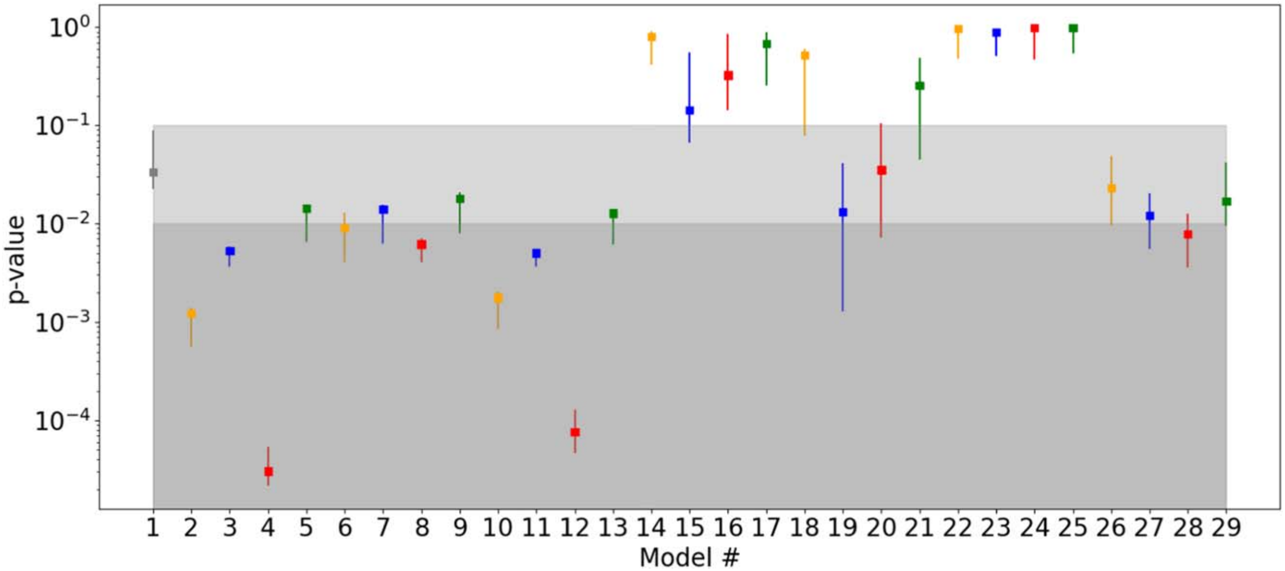

Figure 5. The effect of the redshift uncertainties on the p-values obtained for the selected models. The range displayed is the 90% confidence interval on the p-value. The gray shaded area represents the threshold below which models are rejected, set to 1%.

$\eta(z) = \eta_0(1+z)^{0.6}$, similar to Salvaterra et al. 2012). It can also be assumed that the BBH production is favored at low metallicity, meaning that the evolution of $\eta(z)$ is inversely proportional to the metallicity evolution ($\eta(z) = \eta_0 10^{0.15z}$, using the metallicity evolution from Li 2008). In both models, this factor boosts the BBH density evolution by a factor × 2 at $z = 2$ compared to the LGRBs.

Given the two equations above, it is possible to compute the fraction η_0 as:

$$\eta_0 = \frac{\rho(z_0)}{f_{\rm b}} \times \left(\int_{z_0}^{\infty} \mathcal{R}_{\rm GRB}(z)\, f(z, z_0) \frac{{\rm d}T_c}{{\rm d}z} {\rm d}z\right)^{-1}. \qquad (15)$$

3.2. Results

Figure 6 shows the values of η_0 calculated for the seven favored models in the previous section, for two values of the GRB beaming factor, $f_{\rm b} = 250$ and $f_{\rm b} = 70$, respectively, corresponding to jet opening angles of about 5° and 9°. In the remainder of the discussion, we consider $f_{\rm b} = 250$ as a typical value (Goldstein et al. 2016; Tsvetkova et al. 2017; Lamb et al. 2021), while $f_{\rm b} = 70$ is to be considered as a lower bound to the beaming factor. For the BBH merger rate $\rho(z_0)$, we adopt the value given in the GWTC-3 catalog (The LIGO Scientific Collaboration et al. 2021a), $\rho(z_0 = 0.2) =$ 19–41Gpc^{-3} yr^{-1}. Taking into account the uncertainties on the LVC BBH merger local density rate, Equation (15) gives a large range of predictions for η_0, ranging from ∼0.01 to ∼1 (see Figure 6). Considering the beaming factor $f_{\rm b} = 250$, the value of η_0 is typically a few percent for the models $\mathcal{R}_{16}$, $\mathcal{R}_{21}$, $\mathcal{R}_{23}$, and $\mathcal{R}_{25}$, going up to 10% for the models $\mathcal{R}_{15}$ and $\mathcal{R}_{17}$, and as low as a few tenths of a percent for the model $\mathcal{R}_{24}$. The values for the beaming factor $f_{\rm b} = 70$ are about three times larger. We note that for the models $\mathcal{R}_{15}$, $\mathcal{R}_{16}$, and $\mathcal{R}_{17}$, the delay between the GRB and the merger follows a power law with $dT_{\rm min} = 5$ Gyr, meaning that there are no mergers within the 5 Gyr following an LGRB. These models, while acceptable from a statistical point of view, seem to be unrealistic from an astrophysical point of view.

Figure 6 also shows that this ratio is below 1 for all acceptable models with $f_{\rm b}$ larger than 70. If BBH mergers and LGRBs come from the same BH population, BBH mergers must be rarer than LGRBs. Considering $f_{\rm b} = 250$, as previously justified, the BHs in BBH mergers may represent a few percent of those produced in LGRBs at most. The vast majority of the BHs produced in LGRBs do not end their lives in BBH mergers.

4. Discussion

4.1. Constraints on the BBH Merger Population

Section 2 shows that BBH mergers and LGRBs cannot have the same formation history, unless BBH mergers have a long coalescence time of several Gyr. We briefly discuss this assumption here. Since the LGRB formation rate peaks about 2–3 Gyr after the big bang, models that consider a delay of $t_{\rm d}$ Gyr between the GRB and the merger predict a peak in mergers at 3+$t_{\rm d}$ Gyr after the big bang. For values of $t_{\rm d}$ smaller than 5 Gyr, this peak occurs beyond the horizon of the GW interferometers, leading to a BBH rate that steadily increases with the redshift in the range of the current GW interferometers; such models are not compatible with the data. On the other hand, models with a longer delay ($t_{\rm d} \approx 5$–6 Gyr), which lead to a peak in BBH merger formation at redshift $z \approx 0.5$–0.6, appear to be favored by the data. These models imply a decrease in BBH mergers beyond the peak (Figure 2(c)), providing a direct means for testing the assumption that BBH mergers and LGRBs have progenitors with the same formation history.

Most evolutionary models of BBH mergers, however, predict a delay function following a power law with steep index α and low $dT_{\rm min}$, and a mean delay time close to ∼1 Gyr (e.g., Dominik et al. 2012), even if other studies suggest that a delay time of several Gyr might also be possible for BH–BH systems (Peters 1964; Abbott et al. 2016; Broekgaarden et al. 2021). Since coalescence times of several Gyr are hardly credible, we conclude that BBH mergers and LGRBs do not have the same formation history. This conclusion needs to be

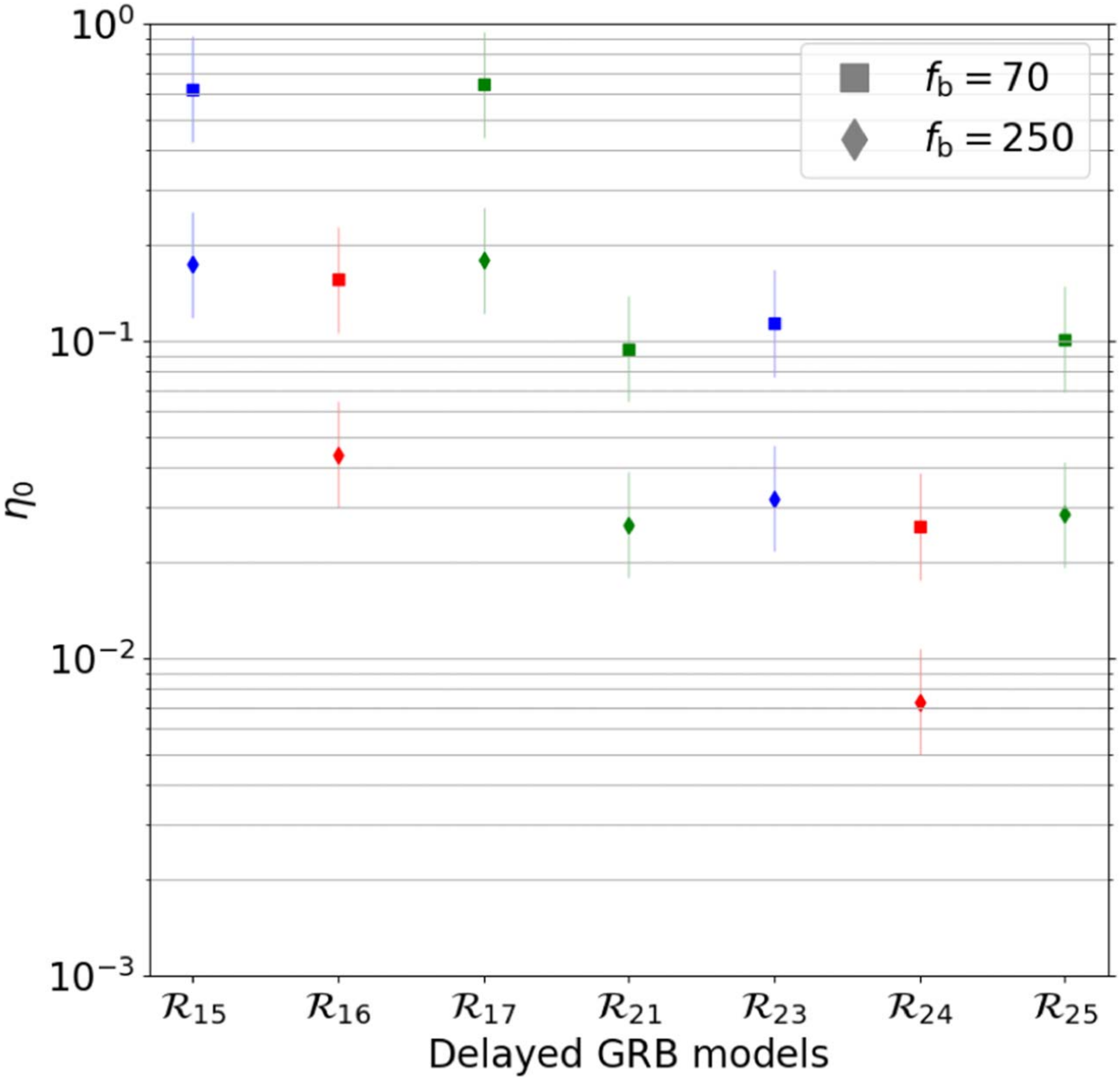

Figure 6. The rate of BBH mergers in units of the LGRB rate, for the seven favored GRB models. The error reflects the incertitude on the value of $\rho(z_0 = 0.2)$. The marker shapes represent the combinations of the beaming factors ($f_b = 70$ or 250).

confirmed with larger BBH merger samples, of course, which will become available in the near future, with runs O4 and O5.

In Section 3, we compare the rate of BBH mergers measured by the LVC collaboration with the rate of LGRBs. Assuming again that BBH mergers and LGRBs have the same formation history, we show that BBH mergers are rarer than LGRBs: for example, taking the model $\mathcal{R}_{25}$ and a standard value for the beaming factor $f_b = 250$, the normalization factor η_0 is between 2% and 4%. If the two populations share the same formation history, several percent of the LGRBs suffice to explain the measured rate of BBH mergers; and if not, this is an indication of a lack of connection between LGRBs and BBH mergers. In both cases, the large majority of the BHs born in LGRBs do not end their lives in BBH mergers.

Taken together, these two studies suggest that BBH mergers and LGRBs have distinct progenitors, and that LGRBs are more frequent than BBH mergers.

4.2. The Nature of LGRB Progenitors

One of the surprises of the LVC detections was the dominance of BHs with low spin. This tells us that the cores of massive stars have lost most of their angular momentum when they collapse into a BH. The core angular momentum has been transferred to the stellar envelope that has been ejected. This is an indication of the efficient transport of angular momentum in the progenitors of BBH mergers, and possibly in most massive stars (Olejak & Belczynski 2021; Bavera et al. 2022; Fuller & Lu 2022). If this scenario is correct, LGRBs, which require stellar cores with a large angular momentum at BH creation, cannot be emitted by single massive stars, nor by massive stars in wide binary systems. According to Kushnir et al. (2017), Piran & Piran (2020), Bavera et al. (2020), Belczynski et al. (2020), and Marchant et al. (2021), the best way for a massive stellar core to keep a large angular momentum until it becomes a BH is through tidal spin-up in a

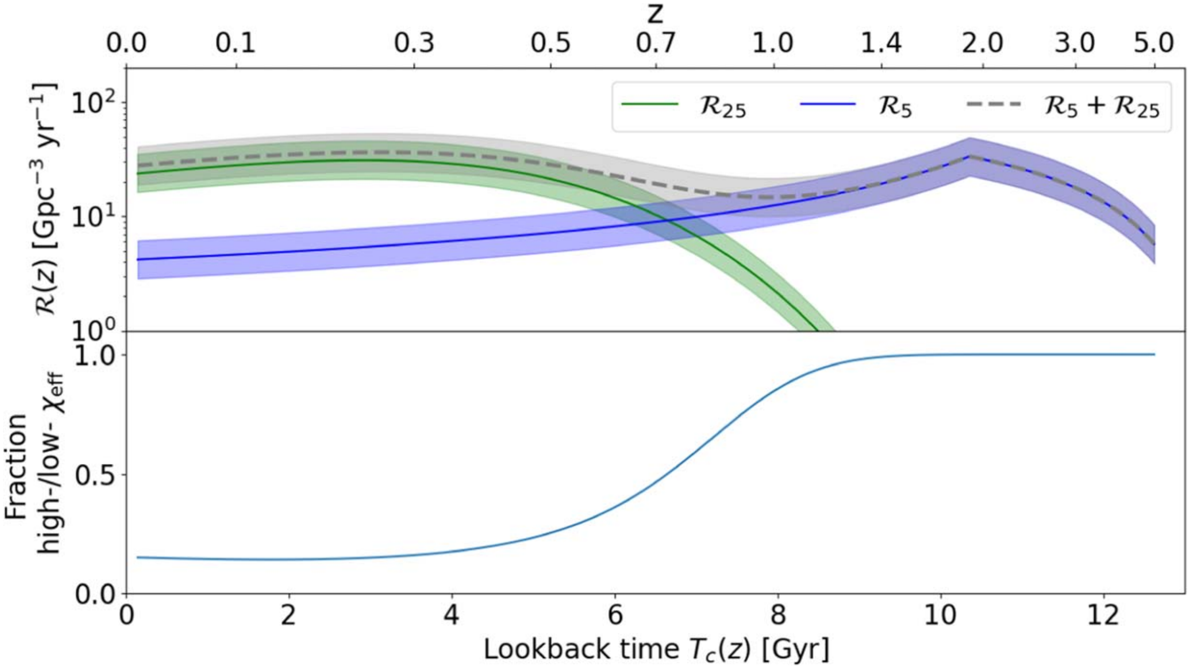

Figure 7. Illustration of the potential two populations: the rate density presented in the top panel is composed of a high-delay (low-spin) population (85%) and a low-delay (high-spin) population (15%), with the sum of the two being illustrated by the dashed gray line. The bottom panel illustrates the evolution of the high-spin fraction of the BBH mergers relative to redshift.

compact system, which is bound to merge after some time. In this model, the population of LGRBs and BBHs (or at least a subsample of the latter) would therefore share common progenitors.

Bavera et al. (2022) have recently published a study using binary stellar evolution and population synthesis calculations to explain the subpopulation of spinning merging BBHs and the emission of LGRBs at BH formation. They reach the conclusion that the progenitors of fast-spinning BBH mergers, formed via isolated binary evolution, likely make a major contribution to the observed rate of luminous LGRBs.

This conclusion differs from the results obtained in this paper, as we propose different origins for BBH mergers and LGRBs. This tension can be explained as follows.

1. The population of BH progenitors generated by Bavera et al. (2022) for the production of LGRBs is based on a value close to the upper limit of the local rate measured by LVC, $\rho(z_0 = 0) = 38.3$ Gpc^{-3} yr^{-1}. We have taken the logarithmic mean of the upper and lower limits ($\rho(z_0 = 0.2) = 28$ Gpc^{-3} yr^{-1}), which is smaller.
2. The SHOALS survey that is used as a reference for the LGRB distribution in Bavera et al. (2022) gives the local rate of the observed GRBs as ~ 0.2 Gpc^{-3} yr^{-1}, while the ones used in this paper are larger, and closer to 1 Gpc^{-3} yr^{-1}.
3. Bavera et al. (2022) use a beaming fraction of 0.05 (corresponding to a beaming factor of $f_b = 20$ or a jet opening angle of $\theta_j \sim 18°$), while we consider a larger beaming factor, by a factor of ∼3–12. Goldstein et al. (2016) show that the distribution of the jet opening angles derived from the prompt emission of 638 GRBs observed by the Fermi Gamma-ray Burst Monitor (GBM) ∼6° or $f_b = 180$, and Tsvetkova et al. (2017) find a median opening angle of $\theta_j \sim 4°$ ($f_b = 400$), based on the breaks in the afterglows of 43 bright GRBs detected by KONUS. Independent measurements obtained by Lamb et al. (2021) on long GRB afterglows also seem to point toward a jet opening angle of around ∼5° ($f_b = 260$). As the beaming factor is directly connected to the true GRB rate, the different values taken by Bavera et al. (2022) and by us explain the different results.

These three factors, which all go in the same direction, lead to a ratio of ∼100 between the long GRB rate used by Bavera et al. (2022) and the one we use. This explains why we find that a small fraction, at most, of LGRBs could be associated with BBH mergers, while Bavera et al. (2022) propose to associate all long GRBs with the subpopulation of BBH mergers with nonzero spin. In the rest of this discussion, we consider that our LGRB models (including the beaming factor) are realistic, and we discuss our findings in this context.

If the majority of LGRBs do not end their lives in BBH mergers, they cannot be produced in compact binary systems and must be emitted by single stars (e.g., Aguilera-Dena et al. 2020) or in binary systems that do not merge. It may be natural to associate them with systems like the X-ray binaries (low-mass X-ray binaries and high-mass X-ray binaries) found in the galaxy, such as Cygnus X-1 (Zhao et al. 2021; Krawczynski & Beheshtipour 2022), GRS 1915+105 (Shreeram & Ingram 2020), or EXO 1846-031 (Draghis et al. 2020), which are rapidly spinning and could be the descendants of LGRBs (although Belczynski et al. 2021 show that the BH spin determination can be subject to systematic effects). The detection of such systems, especially HMXBs, for which accretion spin-up is limited by the lifetime of the secondary star (e.g., Wong et al. 2012), requires the birth of highly spinning BHs (Qin et al. 2019; Miller-Jones et al. 2021), an expected characteristic of LGRB descendants. Nonetheless, it is also possible that LGRB descendants are partitioned in several populations, X-ray binaries being only a subset of them.

4.3. Short-lived LGRB Descendants in the BBH Merger Population?

While our analysis suggests that the majority of BBH mergers have no direct connection with LGRBs, it does not preclude the existence of a small fraction of GRB descendants, with nonzero spin and short merging times, among BBH mergers. Such systems could be produced during a phase of tidal spin-up in a compact system of two massive stars (or a BH and a massive star), as proposed by Bavera et al. (2022). We show here that the addition of a minority fraction of short-lived GRB descendants to a favored model does not change its acceptability.

For illustration, we have constructed a mixed model, consisting of 85% of sources following the model $\mathcal{R}_{25}$ and 15% of sources following the GRB distribution of Palmerio & Daigne (2021; model $\mathcal{R}_5$). The fraction used roughly corresponds to the fraction of BBH mergers in our sample, with χ_{eff} consistent with being positive. This mixed model, shown in Figure 7, is acceptable for the $N/N_{\max}$ test ($p = 0.90$). It requires the following fractions of the GRB population to explain the two components of the model: 3% for the sources following the $\mathcal{R}_{25}$ distribution and 2% for the sources following the Palmerio & Daigne (2021) distribution ($\mathcal{R}_5$).

The addition of a subpopulation of GRB descendants with short merging times has an interesting consequence: this population becomes dominant beyond a certain redshift ($z \approx 0.7$ in Figure 7). This is the consequence of the weak evolution of BBH mergers (see Section 2) compared with the strong evolution of GRBs. This provides a test for the existence of a fraction of direct GRB descendants with short merging times among BBH mergers. If this population exists, it may become dominant at intermediate redshifts and start to be detectable in runs O4 and O5.

Another prediction of GRBs exploding in compact binary systems is the possibility of precessing BHs and precessing GRB jets, which may leave an imprint on the prompt emission or the afterglow of some LGRBs. This possibility has been discussed by various authors, in different contexts (Blackman et al. 1996; Fargion & Grossi 2006; Huang & Liu 2021).

5. Conclusion and Perspectives

With the increasing number of stellar-mass BH detections, population studies become effective for the comparison of their various subclasses. Section 2 shows a comparison between the BBH merger population and a BH population traced by LGRBs, revealing that their redshift distributions are compatible only if we consider a delay of several Gyr between the occurrence of the LGRBs and the BBH mergers. Section 3 shows that for most of the compatible models, the BBH merger progenitor density rate represents less than 10% of the LGRB density rate. These two results are interpreted in Section 4.1 as an indication that BBH mergers and LGRBs have distinct progenitors, with the proposal that the descendants of LGRBs could more resemble the BHs found in galactic X-ray binaries than those in BBH mergers (Section 4.2).

After the publication of GWTC-2, various authors have underlined the fact that BBH mergers may not comprise a single population (e.g., Bouffanais et al. 2021; Hütsi et al. 2021; Zevin et al. 2021), but rather constitute a mix of BH populations originating from isolated stellar binaries, dynamic mergers, and possibly primordial BHs. This claim, however, has been challenged by other authors (e.g., Belczynski et al. 2022; Broekgaarden et al. 2021). The same is true for LGRBs, which can have different "engines," a BH or a fast-rotating magnetar (e.g., Bernardini 2015), and which encompass various subclasses like X-ray flashes, low-luminosity GRBs, choked GRBs, ultra-LGRBs, or LGRBs with a plateau in their afterglow. Future samples of BBH mergers with better statistics will permit the sorting out of these subpopulations, which are expected to have different mass, spin, and redshift distributions. It will then be possible to correlate GRBs with theoretically or empirically defined BBH merger subclasses (e.g., BBH mergers with nonzero effective spin, within a given mass range), obtaining more insight into the physical connections between these phenomena.

In this context, larger samples of BBH mergers and GRBs with redshifts originating from various subclasses will permit population studies of these subclasses, providing insight into the zoo of astrophysical BHs. For example, Section 4.3 has shown a test for the existence of a subpopulation of BBH mergers that would be descendants from LGRBs. Larger samples of BBH mergers are expected, given the increasing sensitivity of GW interferometers (Abbott et al. 2018), and larger samples of GRBs with redshifts will be provided by current and future GRB missions doing fast localizations, like SWIFT (Gehrels et al. 2004; Barthelmy et al. 2005), FERMI (Meegan et al. 2009), INTEGRAL (Lebrun et al. 2003; Mereghetti et al. 2003; Winkler et al. 2003), GECAM (Lv et al. 2018), or the coming SVOM (Godet et al. 2014; Wei et al. 2016; Arcier et al. 2020).

In parallel with these studies, it is essential to develop models of stellar evolution designed to follow the evolution of massive stars up to the production of BHs and their manifestations, like GRBs and BBH mergers (see, for instance, Bavera et al. 2022). Only with such models guiding us will we be able to obtain all the knowledge that can be extracted from the diversity of BH manifestations that are being revealed by present-day instruments.

The authors thank the referee for helpful comments on the evolution of binary systems of massive stars that contributed to improving this paper. The authors are grateful to N. Leroy for helpful discussions regarding the operations of the LIGO and Virgo GW detectors. This work is supported by CNES and the Paul Sabatier University.

Software: NumPy (van der Walt et al. 2011), SciPy (Virtanen et al. 2020), Matplotlib (Hunter 2007), Astropy (Astropy Collaboration et al. 2013), LALSuite (LIGO Scientific Collaboration 2018).

Appendix
Horizon Redshift Calculation

Table 2 gives the properties of the 79 BBH events used in this work, in addition to the horizons computed with the method provided in Section 2.1.

Table 2

BBH Mergers Used in This Paper from Abbott et al. (2019, 2021a) and The LIGO Scientific Collaboration et al. (2021b), with the Original S/N and Calculated Horizon Redshift z_h Thanks to Equation (3)

Name	$m_1(M_\odot)$	$m_2(M_\odot)$	S/N	z	z_h	V_{max}/V
GW200316_215756◆	13.1	7.8	10.3	$0.22^{+0.08}_{-0.08}$	$0.28^{+0.10}_{-0.10}$	2.05
GW200311_115853◆	34.2	27.7	17.8	$0.23^{+0.05}_{-0.07}$	$0.53^{+0.12}_{-0.17}$	9.59
GW200302_015811◆	37.8	20.0	10.8	$0.28^{+0.16}_{-0.12}$	$0.38^{+0.22}_{-0.17}$	2.33
GW200225_060421◆	19.3	14.0	12.5	$0.22^{+0.09}_{-0.10}$	$0.35^{+0.15}_{-0.16}$	3.55
GW200224_222234◆	40.0	32.5	20.0	$0.32^{+0.08}_{-0.11}$	$0.86^{+0.24}_{-0.33}$	12.34
GW200220_124850◆	38.9	27.9	8.5	$0.66^{+0.36}_{-0.31}$	$0.71^{+0.39}_{-0.33}$	1.18
GW200219_094415◆	37.5	27.9	10.7	$0.57^{+0.22}_{-0.22}$	$0.79^{+0.32}_{-0.32}$	2.19
GW200216_220804◆	51.0	30.0	8.1	$0.63^{+0.37}_{-0.29}$	$0.64^{+0.37}_{-0.29}$	1.03
GW200210_092254◆	24.1	2.8	8.4	$0.19^{+0.08}_{-0.06}$	$0.20^{+0.08}_{-0.06}$	1.14
GW200209_085452◆	35.6	27.1	9.6	$0.57^{+0.25}_{-0.26}$	$0.70^{+0.32}_{-0.33}$	1.64
GW200208_130117◆	37.8	27.4	10.8	$0.40^{+0.15}_{-0.14}$	$0.55^{+0.21}_{-0.20}$	2.30
GW200202_154313◆	10.1	7.3	10.8	$0.09^{+0.03}_{-0.03}$	$0.12^{+0.04}_{-0.04}$	2.41
GW200129_065458◆	34.5	28.9	26.8	$0.18^{+0.05}_{-0.07}$	$0.64^{+0.20}_{-0.28}$	30.53
GW200128_022011◆	42.2	32.6	10.6	$0.56^{+0.28}_{-0.28}$	$0.76^{+0.39}_{-0.39}$	2.13
GW200112_155838◆	35.6	28.3	19.8	$0.24^{+0.07}_{-0.08}$	$0.62^{+0.20}_{-0.23}$	12.76
GW191230_180458◆	49.4	37.0	10.4	$0.69^{+0.26}_{-0.27}$	$0.92^{+0.35}_{-0.36}$	1.95
GW191222_033537◆	45.1	34.7	12.5	$0.51^{+0.23}_{-0.26}$	$0.83^{+0.39}_{-0.44}$	3.28
GW191216_213338◆	12.1	7.7	18.6	$0.07^{+0.02}_{-0.03}$	$0.16^{+0.05}_{-0.07}$	11.78
GW191215_223052◆	24.9	18.1	11.2	$0.35^{+0.13}_{-0.14}$	$0.50^{+0.19}_{-0.21}$	2.56
GW191204_171526◆	11.9	8.2	17.5	$0.13^{+0.04}_{-0.05}$	$0.29^{+0.09}_{-0.11}$	9.48
GW191204_110529◆	27.3	19.3	8.8	$0.34^{+0.25}_{-0.18}$	$0.38^{+0.28}_{-0.20}$	1.31
GW191129_134029◆	10.7	6.7	13.1	$0.16^{+0.05}_{-0.06}$	$0.26^{+0.08}_{-0.10}$	4.11
GW191127_050227◆	53.0	24.0	9.2	$0.57^{+0.40}_{-0.29}$	$0.66^{+0.47}_{-0.34}$	1.45
GW191126_115259◆	12.1	8.3	8.3	$0.30^{+0.12}_{-0.13}$	$0.31^{+0.13}_{-0.14}$	1.11
GW191109_010717◆	65.0	47.0	17.3	$0.25^{+0.18}_{-0.12}$	$0.55^{+0.39}_{-0.26}$	8.22
GW191105_143521◆	10.7	7.7	9.7	$0.23^{+0.07}_{-0.09}$	$0.28^{+0.09}_{-0.11}$	1.73
GW191103_012549◆	11.8	7.9	8.9	$0.20^{+0.09}_{-0.09}$	$0.22^{+0.10}_{-0.10}$	1.36
GW190930_133541■	12.3	7.8	9.8	$0.15^{+0.06}_{-0.06}$	$0.18^{+0.07}_{-0.07}$	1.82
GW190929_012149■	80.8	24.1	9.9	$0.38^{+0.49}_{-0.17}$	$0.47^{+0.59}_{-0.21}$	1.74
GW190926_050336■	39.8	23.2	9.0	$0.62^{+0.40}_{-0.29}$	$0.71^{+0.47}_{-0.34}$	1.37
GW190925_232845■	21.2	15.6	9.9	$0.19^{+0.07}_{-0.07}$	$0.24^{+0.09}_{-0.09}$	1.83
GW190924_021846■	8.9	5.0	13.2	$0.12^{+0.04}_{-0.04}$	$0.20^{+0.07}_{-0.07}$	4.23
GW190916_200658■	44.3	23.9	8.2	$0.71^{+0.46}_{-0.36}$	$0.73^{+0.47}_{-0.37}$	1.07
GW190915_235702■	35.3	24.4	13.1	$0.30^{+0.11}_{-0.10}$	$0.50^{+0.19}_{-0.18}$	3.96
GW190910_112807■	43.9	35.6	13.4	$0.28^{+0.16}_{-0.10}$	$0.48^{+0.29}_{-0.18}$	4.27
GW190909_114149■	45.8	28.3	9.0	$0.62^{+0.41}_{-0.33}$	$0.71^{+0.47}_{-0.38}$	1.39
GW190828_065509■	24.1	10.2	11.1	$0.30^{+0.10}_{-0.10}$	$0.42^{+0.14}_{-0.14}$	2.50
GW190828_063405■	32.1	26.2	16.0	$0.38^{+0.10}_{-0.15}$	$0.81^{+0.24}_{-0.36}$	6.76
GW190814■	23.2	2.6	22.2	$0.05^{+0.01}_{-0.01}$	$0.14^{+0.02}_{-0.03}$	19.29
GW190805_211137■	48.2	32.0	8.3	$0.82^{+0.48}_{-0.40}$	$0.85^{+0.50}_{-0.41}$	1.08
GW190803_022701■	37.3	27.3	8.6	$0.55^{+0.26}_{-0.24}$	$0.60^{+0.29}_{-0.26}$	1.22
GW190731_140936■	41.5	28.8	8.5	$0.55^{+0.31}_{-0.26}$	$0.58^{+0.33}_{-0.28}$	1.16
GW190728_064510■	12.3	8.1	13.6	$0.18^{+0.05}_{-0.07}$	$0.31^{+0.09}_{-0.12}$	4.58
GW190727_060333■	38.0	29.4	12.3	$0.55^{+0.21}_{-0.22}$	$0.89^{+0.36}_{-0.38}$	3.16
GW190725_174728■	11.5	6.4	9.1	$0.21^{+0.10}_{-0.09}$	$0.24^{+0.11}_{-0.10}$	1.43
GW190720_000836■	13.4	7.8	11.7	$0.16^{+0.12}_{-0.06}$	$0.23^{+0.18}_{-0.09}$	2.97
GW190708_232457■	17.6	13.2	13.1	$0.18^{+0.06}_{-0.07}$	$0.30^{+0.10}_{-0.12}$	4.07
GW190707_093326■	11.6	8.4	13.0	$0.16^{+0.07}_{-0.07}$	$0.26^{+0.12}_{-0.12}$	4.00
GW190706_222641■	67.0	38.2	12.3	$0.71^{+0.32}_{-0.27}$	$1.10^{+0.45}_{-0.38}$	2.70
GW190701_203306■	53.9	40.8	11.6	$0.37^{+0.11}_{-0.12}$	$0.54^{+0.16}_{-0.18}$	2.75
GW190630_185205■	35.1	23.7	15.6	$0.18^{+0.10}_{-0.07}$	$0.36^{+0.21}_{-0.15}$	6.81
GW190620_030421■	57.1	35.5	10.9	$0.49^{+0.23}_{-0.20}$	$0.68^{+0.32}_{-0.28}$	2.28
GW190602_175927■	69.1	47.8	12.1	$0.47^{+0.25}_{-0.17}$	$0.71^{+0.36}_{-0.25}$	2.86
GW190527_092055■	36.5	22.6	8.9	$0.44^{+0.34}_{-0.20}$	$0.49^{+0.39}_{-0.23}$	1.33
GW190521_074359■	42.2	32.8	24.4	$0.24^{+0.07}_{-0.10}$	$0.78^{+0.25}_{-0.36}$	22.02
GW190521■	95.3	69.0	14.4	$0.64^{+0.28}_{-0.28}$	$1.08^{+0.40}_{-0.40}$	3.36
GW190519_153544■	66.0	40.5	12.0	$0.44^{+0.25}_{-0.14}$	$0.67^{+0.37}_{-0.21}$	2.90

Table 2
(Continued)

Name	$m_1(M_\odot)$	$m_2(M_\odot)$	S/N	z	z_h	V_max/V
GW190517_055101■	37.4	25.3	10.2	$0.34^{+0.24}_{-0.14}$	$0.44^{+0.32}_{-0.19}$	2.00
GW190514_065416■	39.0	28.4	8.3	$0.67^{+0.33}_{-0.31}$	$0.70^{+0.35}_{-0.33}$	1.10
GW190513_205428■	35.7	18.0	12.3	$0.37^{+0.13}_{-0.13}$	$0.58^{+0.22}_{-0.22}$	3.25
GW190512_180714■	23.3	12.6	12.3	$0.27^{+0.09}_{-0.10}$	$0.42^{+0.14}_{-0.16}$	3.31
GW190503_185404■	43.3	28.4	12.1	$0.27^{+0.11}_{-0.11}$	$0.41^{+0.17}_{-0.17}$	3.21
GW190426_190642■	106.9	76.6	9.6	$0.70^{+0.41}_{-0.30}$	$0.82^{+0.46}_{-0.34}$	1.45
GW190424_180648■	40.5	31.8	10.1	$0.39^{+0.23}_{-0.19}$	$0.50^{+0.30}_{-0.25}$	1.91
GW190421_213856■	41.3	31.9	10.6	$0.49^{+0.19}_{-0.21}$	$0.66^{+0.27}_{-0.29}$	2.12
GW190413_134308■	47.5	31.8	9.0	$0.71^{+0.31}_{-0.30}$	$0.81^{+0.36}_{-0.34}$	1.37
GW190413_052954■	34.7	23.7	8.6	$0.59^{+0.29}_{-0.24}$	$0.63^{+0.32}_{-0.26}$	1.20
GW190412■	30.1	8.3	18.9	$0.15^{+0.03}_{-0.03}$	$0.35^{+0.07}_{-0.07}$	11.12
GW190408_181802■	24.6	18.4	14.7	$0.29^{+0.06}_{-0.10}$	$0.55^{+0.12}_{-0.20}$	5.48
GW170823$^{\mathrm{O}}$	39.5	29.0	11.5	$0.35^{+0.15}_{-0.15}$	$0.51^{+0.23}_{-0.23}$	2.75
GW170818$^{\mathrm{O}}$	35.4	26.7	11.3	$0.21^{+0.07}_{-0.07}$	$0.30^{+0.10}_{-0.10}$	2.69
GW170814$^{\mathrm{O}}$	30.6	25.2	15.9	$0.12^{+0.03}_{-0.04}$	$0.24^{+0.06}_{-0.08}$	7.36
GW170809$^{\mathrm{O}}$	35.0	23.8	12.4	$0.20^{+0.05}_{-0.07}$	$0.31^{+0.08}_{-0.11}$	3.51
GW170729$^{\mathrm{O}}$	50.2	34.0	10.2	$0.49^{+0.19}_{-0.21}$	$0.63^{+0.25}_{-0.28}$	1.92
GW170608$^{\mathrm{O}}$	11.0	7.6	14.9	$0.07^{+0.02}_{-0.02}$	$0.13^{+0.04}_{-0.04}$	6.20
GW170104$^{\mathrm{O}}$	30.8	20.0	13.0	$0.20^{+0.08}_{-0.08}$	$0.33^{+0.14}_{-0.14}$	4.01
GW151226$^{\mathrm{O}}$	13.7	7.7	13.1	$0.09^{+0.04}_{-0.04}$	$0.15^{+0.07}_{-0.07}$	4.22
GW151012$^{\mathrm{O}}$	23.2	13.6	10.0	$0.21^{+0.09}_{-0.09}$	$0.26^{+0.11}_{-0.11}$	1.89
GW150914$^{\mathrm{O}}$	35.6	30.6	24.4	$0.09^{+0.03}_{-0.03}$	$0.28^{+0.10}_{-0.10}$	25.65

Note. Errors are given at the 90% confidence interval. GW events with O, ■, and ◆ are from GWTC-1, GWTC-2, and GWTC-3, respectively.

ORCID iDs

Benjamin Arcier https://orcid.org/0000-0001-5043-0699
Jean-Luc Atteia https://orcid.org/0000-0001-7346-5114

References

Abbott, B. P., Abbott, R., Abbott, T. D., et al. 2016, PhRvL, 116, 061102
Abbott, B. P., Abbott, R., Abbott, T. D., et al. 2018, LRR, 21, 3
Abbott, B. P., Abbott, R., Abbott, T. D., et al. 2019, PhRvX, 9, 031040
Abbott, R., Abbott, T. D., Abraham, S., et al. 2021a, PhRvX, 11, 021053
Abbott, R., Abbott, T. D., Abraham, S., et al. 2021b, ApJL, 913, L7
Aguilera-Dena, D. R., Langer, N., Antoniadis, J., & Müller, B. 2020, ApJ, 901, 114
Arcier, B., Atteia, J. L., Godet, O., et al. 2020, Ap&SS, 365, 185
Astropy Collaboration, Robitaille, T. P., Tollerud, E. J., et al. 2013, A&A, 558, A33
Atteia, J. L., Dezalay, J. P., Godet, O., et al. 2018, A&A, 610, A58
Atteia, J. L., Heussaff, V., Dezalay, J. P., et al. 2017, ApJ, 837, 119
Barthelmy, S. D., Barbier, L. M., Cummings, J. R., et al. 2005, SSRv, 120, 143
Bartos, I., Kocsis, B., Haiman, Z., & Márka, S. 2017, ApJ, 835, 165
Bavera, S. S., Fragos, T., Qin, Y., et al. 2020, A&A, 635, A97
Bavera, S. S., Fragos, T., Zapartas, E., et al. 2022, A&A, 657, L8
Belczynski, K., Done, C., & Lasota, J. P. 2021, arXiv:2111.09401
Belczynski, K., Holz, D. E., Bulik, T., & O'Shaughnessy, R. 2016, Natur, 534, 512
Belczynski, K., Klencki, J., Fields, C. E., et al. 2020, A&A, 636, A104
Belczynski, K., Romagnolo, A., Olejak, A., et al. 2022, ApJ, 925, 69
Bernardini, M. G. 2015, JHEAp, 7, 64
Blackman, E. G., Yi, I., & Field, G. B. 1996, ApJL, 473, L79
Bouffanais, Y., Mapelli, M., Santoliquido, F., et al. 2021, arXiv:2102.12495
Broekgaarden, F. S., Berger, E., Stevenson, S., et al. 2021, arXiv:2112.05763
Chen, H.-Y., Holz, D. E., Miller, J., et al. 2021, CQGra, 38, 055010
Chrimes, A. A., Stanway, E. R., & Eldridge, J. J. 2020, MNRAS, 491, 3479
Condon, J. J., & Matthews, A. M. 2018, PASP, 130, 073001
De Luca, V., Franciolini, G., Pani, P., & Riotto, A. 2021, JCAP, 2021, 003
Dominik, M., Belczynski, K., Fryer, C., et al. 2012, ApJ, 759, 52
Draghis, P. A., Miller, J. M., Cackett, E. M., et al. 2020, ApJ, 900, 78
Fargion, D., & Grossi, M. 2006, ChJAS, 6, 342
Farris, B. D., Liu, Y. T., & Shapiro, S. L. 2010, PhRvD, 81, 084008
Fuller, J., & Lu, W. 2022, MNRAS, 511, 3951
Galama, T. J., Vreeswijk, P. M., van Paradijs, J., et al. 1998, Natur, 395, 670
Gehrels, N., Chincarini, G., Giommi, P., et al. 2004, ApJ, 611, 1005
Godet, O., Nasser, G., Atteia, J. L., et al. 2014, Proc. SPIE, 9144, 914424
Goldstein, A., Connaughton, V., Briggs, M. S., & Burns, E. 2016, ApJ, 818, 18
Huang, B.-Q., & Liu, T. 2021, ApJ, 916, 71
Hunter, J. D. 2007, CSE, 9, 90
Hütsi, G., Raidal, M., Vaskonen, V., & Veermäe, H. 2021, JCAP, 2021, 068
Krawczynski, H., & Beheshtipour, B. 2022, arXiv:2201.07360
Kushnir, D., Zaldarriaga, M., Kollmeier, J. A., & Waldman, R. 2017, MNRAS, 467, 2146
Lamb, G. P., Kann, D. A., Fernández, J. J., et al. 2021, MNRAS, 506, 4163
Lebrun, F., Leray, J. P., Lavocat, P., et al. 2003, A&A, 411, L141
Levan, A., Crowther, P., de Grijs, R., et al. 2016, SSRv, 202, 33
Li, L.-X. 2008, MNRAS, 388, 1487
Liang, E., Zhang, B., Virgili, F., & Dai, Z. G. 2007, ApJ, 662, 1111
Lien, A., Sakamoto, T., Gehrels, N., et al. 2014, ApJ, 783, 24
LIGO Scientific Collaboration 2018, LIGO Algorithm Library—LALSuite, free software (GPL), doi:10.7935/GT1W-FZ16
Lv, P., Xiong, S. L., Sun, X. L., Lv, J. G., & Li, Y. G. 2018, JInst, 13, P08014
MacFadyen, A. I., & Woosley, S. E. 1999, ApJ, 524, 262
Mao, S., & Paczynski, B. 1992, ApJL, 388, L45
Marchant, P., Pappas, K. M. W., Gallegos-Garcia, M., et al. 2021, A&A, 650, A107
McKernan, B., Ford, K. E. S., & O'Shaughnessy, R. 2020, MNRAS, 498, 4088
Meegan, C., Lichti, G., Bhat, P. N., et al. 2009, ApJ, 702, 791
Mereghetti, S., Götz, D., Borkowski, J., Walter, R., & Pedersen, H. 2003, A&A, 411, L291
Miller-Jones, J. C. A., Bahramian, A., Orosz, J. A., et al. 2021, Sci, 371, 1046
Nakar, E. 2007, PhR, 442, 166
Olejak, A., & Belczynski, K. 2021, ApJL, 921, L2
Palmerio, J. T., & Daigne, F. 2021, A&A, 649, A166
Peters, P. C. 1964, PhRv, 136, 1224
Piran, Z., & Piran, T. 2020, ApJ, 892, 64

Planck Collaboration, Aghanim, N., Akrami, Y., et al. 2020, A&A, 641, A6
Qin, Y., Marchant, P., Fragos, T., Meynet, G., & Kalogera, V. 2019, ApJL, 870, L18
Salvaterra, R., Campana, S., Vergani, S. D., et al. 2012, ApJ, 749, 68
Schmidt, M. 1968, ApJ, 151, 393
Shreeram, S., & Ingram, A. 2020, MNRAS, 492, 405
Soderberg, A. M., Nakar, E., Berger, E., & Kulkarni, S. R. 2006a, ApJ, 638, 930
Soderberg, A. M., Kulkarni, S. R., Nakar, E., et al. 2006b, Natur, 442, 1014
Tagliaferri, G., Malesani, D., Chincarini, G., et al. 2006, AdSpR, 38, 1295
The LIGO Scientific Collaboration, The Virgo Collaboration, & The KAGRA Scientific Collaboration et al. 2021a, arXiv:2111.03634
The LIGO Scientific Collaboration, the Virgo Collaboration, the KAGRA Collaboration, et al. 2021b, arXiv:2111.03606
The LIGO Scientific Collaboration, the Virgo Collaboration, Abbott, R., et al. 2021c, arXiv:2108.01045
Tsvetkova, A., Frederiks, D., Golenetskii, S., et al. 2017, ApJ, 850, 161
van der Walt, S., Colbert, S. C., & Varoquaux, G. 2011, CSE, 13, 22
Vedrenne, G., & Atteia, J.-L. 2009, Gamma-Ray Bursts (Berlin: Springer Verlag)
Virtanen, P., Gommers, R., Oliphant, T. E., et al. 2020, NatMe, 17, 261
Wanderman, D., & Piran, T. 2010, MNRAS, 406, 1944
Wanderman, D., & Piran, T. 2015, MNRAS, 448, 3026
Wang, Y.-Z., Fan, Y.-Z., Tang, S.-P., Qin, Y., & Wei, D.-M. 2021, arXiv:2110.10838
Wei, J., Cordier, B., Antier, S., et al. 2016, arXiv:1610.06892
Winkler, C., Courvoisier, T. J. L., Di Cocco, G., et al. 2003, A&A, 411, L1
Wong, T.-W., Valsecchi, F., Fragos, T., & Kalogera, V. 2012, ApJ, 747, 111
Woosley, S. E., & Bloom, J. S. 2006, ARA&A, 44, 507
Zevin, M., Bavera, S. S., Berry, C. P. L., et al. 2021, ApJ, 910, 152
Zhao, X., Gou, L., Dong, Y., et al. 2021, ApJ, 908, 117